Results in Engineering 26 (2025) 104998

Contents lists available at ScienceDirect

Results in Engineering

journal homepage: www.sciencedirect.com/journal/results-in-engineering

A multiscale finite element approach to analyse the effect of shot peening-induced surface roughness on fretting fatigue crack initiation

Chao Li [a], Sutao Han [a], Can Wang [a], Auezhan Amanov [b,c], Lihua Wang [d,*], Magd Abdel Wahab [a,e,f,*]

[a] Soete Laboratory, Department of Electromechanical, Systems and Metal Engineering, Faculty of Engineering and Architecture, Ghent University, Belgium
[b] Faculty of Engineering and Natural Sciences, Tampere University, Finland
[c] Department of Mechanical Engineering, Sun Moon University, South Korea
[d] School of Aerospace Engineering and Applied Mechanics, Tongji University, Shanghai 200092, China
[e] College of Engineering, Yuan Ze University, Taiwan, China
[f] Parallel and Distributed Systems Laboratory, Jožef Stefan Institute, Jamova cesta 39, Ljubljana SI-1000, Slovenia

ARTICLE INFO

Keywords:
Shot peening
Surface roughness
Residual stress
Fretting fatigue
Finite element method
Multiscale analysis

ABSTRACT

Shot peening (SP) is a widely used surface treatment technique that enhances the mechanical performance of materials, notably improving fatigue resistance by inducing compressive residual stresses (RS) and modifying surface characteristics. While the overall benefits of SP on fatigue life are well-documented, the specific role of SP-induced surface roughness in fretting fatigue behaviour remains unclear. This study develops a multiscale framework based on finite element method (FEM) to isolate and quantify the influence of surface roughness resulting from SP on fretting fatigue. At the microscale, detailed FEM simulations are conducted to assess how surface topography affects local contact stresses, thereby extracting critical features brought by roughness. These features are then integrated into a macroscale model to construct a SP-treated model that accounts for the effects of surface roughness. Numerical results reveal that while surface roughness has a minimal effect on crack initiation location and orientation, it significantly affects crack initiation lifetime by redistributing contact stresses more favourably. Furthermore, incorporating experimentally measured roughness profiles into the numerical models enhances the accuracy of fatigue life predictions. These findings underscore the importance of considering surface roughness in numerical simulations to achieve reliable predictions of fretting fatigue behaviour in SP-treated materials.

1. Introduction

Fretting fatigue is a complex damage mechanism arising from oscillatory micro-sliding between contacting surfaces under cyclic loading, recognized as a major cause of unexpected failures in mechanical assembly systems [1]. This phenomenon induces highly localized stress concentrations at contact interfaces, drastically accelerating crack initiation even under nominally low applied stresses [2]. The insidious nature of fretting-induced failures poses critical challenges across industries, e.g. aerospace engine components experience fretting at blade-disk joints, automotive transmissions suffer bearing surface degradation, orthopaedic implants develop micromotion-induced cracks, and wind turbine bearings undergo premature spalling [3,4]. Such failures not only require costly component replacements but also carry severe safety hazards, prompting extensive research into effective mitigation strategies [5,6].

Shot peening (SP) has emerged as a highly effective countermeasure, combining operational simplicity with multidimensional surface enhancements. SP induces controlled surface severe plastic deformation (SSPD) in the near-surface region by bombarding the component with high-velocity spherical media (usually steel, ceramic, or glass beads) [7,8]. This process involves the generation of compressive residual stresses (RS), the formation of a work-hardened subsurface layer with a refined microstructure, and the modification of surface topography through dimple formation [9–11]. Unlike subtractive surface treatments such as chemical milling, electrochemical polishing, and sandblasting, SP enhances fatigue resistance without altering component dimensions, which is critical for high-precision applications [12–14]. The

* Corresponding authors.
E-mail addresses: lhwang@tongji.edu.cn (L. Wang), magd.abdelwahab@UGent.be (M. Abdel Wahab).

https://doi.org/10.1016/j.rineng.2025.104998
Received 3 March 2025; Received in revised form 15 April 2025; Accepted 17 April 2025
Available online 18 April 2025

anti-fretting efficacy of SP primarily stems from two interrelated mechanisms. First, the induced compressive RS, typically peaking at 50–150 μm below the surface, is superimposed on the applied stresses, effectively reducing the tensile stress and producing a crack closure effect [10,15,16]. Compressive RS acts as a powerful barrier against fretting wear and fatigue. Experimental studies on Ti-6Al-4 V specimens demonstrated that optimized SP parameters could delay the crack initiation of fretting fatigue compared to untreated surfaces [17]. Although the introduction of RS does not change the starting position of crack initiation, it significantly increases the crack initiation lifetime while affecting the crack direction [18,19]. In addition, RS relaxation is a critical phenomenon, particularly in fretting fatigue, where cyclic loading near high-stress contact zones plays a significant role. While RS, is typically introduced through processes like SP, these stresses are not static and will diminish over time due to cyclic loading [20,21]. Research indicated that the relaxation occurred in two stages, i.e. an initial rapid reduction caused by local plastic deformation and a slower logarithmic reduction over successive cycles due to thermal or mechanical fatigue [22]. For example, cyclic loading can relax RS entirely in the early cycles, particularly in the presence of high initial stress amplitudes. This relaxation process can lead to local stress redistribution, significantly affecting the fatigue performance of material [23].

Second, the stochastic surface roughness alters the contact mechanics-asperity interactions and redistributes pressures over 15–30 % larger nominal areas during initial cycles, reducing initial wear rates by up to 21.3 % [24]. However, after approximately 3,000 cycles, this beneficial effect gradually diminishes as the number of cycles increases. To investigate the role of surface roughness in fretting fatigue, comparative analyses have been conducted on unpolished and polished SP-treated specimens. However, the polishing process typically removes 20–30 μm of surface material, potentially eliminating high-gradient RS near the surface. This complicates the efforts to isolate and rigorously assess the influence of roughness alone. Additionally, polishing alters the coefficient of friction (CoF), which affects the stress distribution and, consequently, fatigue lifespan. It has been shown that surface roughness fragments the contact area into smaller regions, leading to localized stress concentrations. This redistribution reduces the stress intensity factor (SIF) relative to contact between smooth surfaces, ultimately slowing crack growth rate and influencing fretting fatigue behaviour [25]. While analytical methods have been attempted to quantify the influence of roughness on fretting fatigue, they exhibited a statistical variance as high as 75 % [26]. Although the importance of roughness on fatigue life is widely recognized, its complex interaction with fretting fatigue mechanisms remains insufficiently understood.

Finite element method (FEM) has emerged as one of the most versatile and essential tools for the numerical analysis of fretting fatigue [16,27,28]. FEM offers distinct advantages, including the ability to simulate complex loading conditions, capture detailed stress distributions, visualize failure mechanisms, and reduce the development time and cost of fatigue performance analysis [29]. However, when applied to structures with microscale features, FEM can become computationally expensive. Therefore, multiscale analysis has gradually gained attention to bridge the gap between microscopic and macroscopic behaviours. The analysis of microscopic contact under normal load provides a basis for evaluating macroscopic tangential responses and fatigue behaviour [30,31]. Multiscale approaches have also been employed to study the effects of micro-defects (such as micro-cracks and micro-voids) on macroscopic crack propagation, in combination with FEM [32,33]. In addition, multiscale analysis offers insights into the effects of pre-hardening effect on fatigue lifespan [34]. FEM also enables the incorporation of stochastic surface roughness models, which deepen the understanding of how interface morphology influences the macroscopic mechanical response [35,36].

Despite these advancements, the specific impact of SP-induced surface roughness on fretting fatigue remains under-explored. This gap highlights the need for comprehensive studies to explain surface interactions and their effects on fatigue crack initiation. To address this need, this study adopts a multiscale approach that integrates microscale stress analysis with macroscale crack initiation evaluation. By combining macroscale finite element (FE) modeling with detailed microscale simulations, this study presents insights into the role of surface roughness in fretting fatigue. The numerical results, supported by experimental validation, confirm the protective barrier role of surface roughness in delaying crack initiation and extending fretting fatigue lifespan. Furthermore, incorporation of roughness into the FE model significantly enhances the accuracy of fretting fatigue life predictions for SP-treated specimens. These findings offer valuable guidance for the numerical prediction model of fretting fatigue in SP-treated materials.

2. Experimental data

The experimental investigation into the impact of SP on the fretting fatigue behaviour of Al 7075-T651 was conducted and detailed in Ref. [19]. Fig. 1(a) illustrates the experimental setup for fretting fatigue tests, where both the samples and contact pads were made from Al 7075-T651, and the plane samples underwent an SP treatment. Al 7075-T651 has an elastic modulus of 71 GPa and a Poisson's ratio of 0.33. The specimens were treated with a specific SP process designated as 9A-230H-90°. In detail, '9A' indicates a deflection arc height in thousandths of an inch (0.009 inches), reflecting the kinetic energy of the shot stream. '230′ denotes the shot diameter in ten-thousandths of an inch (0.023 inches) with a hardness of 45–50 HRC. '90′ signifies the projection angle (90°) of the balls perpendicular to the surface ensured uniform deformation.

Fig. 1(b) provides a sketch of the samples, offering a visual representation of their characteristics in the fretting fatigue tests. After the SP process, surface roughness was measured using an optical profilometer, the Sensofar S Neox. CoF and various roughness parameters of untreated and SP-treated specimen are summarized in Table 1. Notably, correlation length (ξ) quantifies the rate of roughness variations across spatial coordinates and will be quantified in Section 4.1. It is important to note that the roughness of the contact pads is excluded from this analysis, as their roughness values are at least an order of magnitude lower than those of the specimens. The roughness parameters were derived from the average of three repeated measurements. A detailed explanation of these parameters is provided in Section 4.1.

X-ray diffraction (XRD) was used to measure the RS field in the specimens following the SP treatment. As shown in Fig. 2, RS measurements were taken at various depths beneath the surface of the SP-treated samples. The mean values of these measurements were calculated, with the standard deviation presented as a percentage error. The XRD measurements adhered to the EN 15,305:2008 standard, and the equipment used was the iXRD portable RS analyser from PROTO. Only the RS component in the longitudinal direction (σ_{xx}) of the specimen is reported, as it aligns with the direction of the fretting load and is considered to have a major influence on fatigue performance in this experiment. The beneficial compressive RS depth extends to 0.35 mm below the surface, with the highest concentrations of RS not at the outermost layer, but slightly beneath the surface.

In the fretting fatigue testing setup, the procedure begins by pressing two cylindrical contact pads against a "dog bone" shaped specimen under a constant normal load (P). Subsequently, a cyclic (harmonic) axial stress, denoted as σ_{axial}, is applied to one end of the specimen. This interaction between the contact pads and the specimen generates a cyclic in-phase tangential load (Q) due to contact and friction. The testing machine, equipped with load cells, continuously monitors these loads, enabling the testing of various fretting-load combinations (P, σ_{axial}, and Q). Throughout the tests, the stress ratio of σ_{axial} is maintained at -1.

To comprehensively assess the impact of surface roughness on fretting fatigue behaviour, a diverse set of working conditions is selected, as outlined in Table 2. These conditions cover a range of load amplitude combinations, and their respective number of cycles to failure (N_f). To

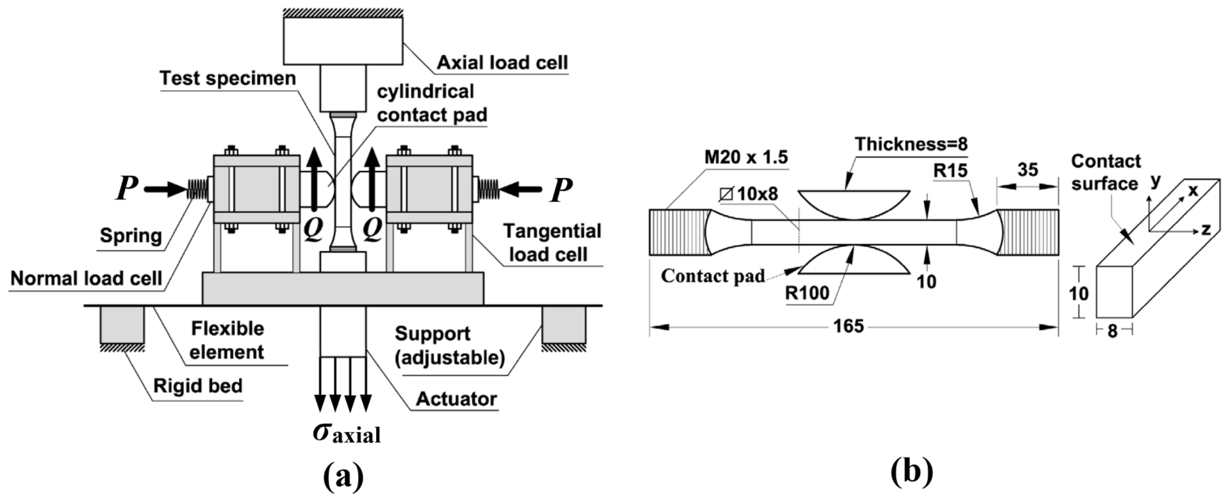

Fig. 1. (a) Schematic representation of the device, and (b) dimensional drawing of the specimen (dimensions in mm) of fretting fatigue tests [19].

Table 1
CoF and surface roughness parameters [19].

Specimens	μ	Roughness		
		R_a [μm]	R_y [μm]	ξ [μm]
As received	0.75	0.23	1.60	–
Shot-peened	0.85	5.59	35.21	139.9
Contact pad	–	0.13	1.53	–

Table 2
Experimental fretting fatigue lives under different loading combinations [19].

Load No.	P [N]	σ_{axial} [MPa]	Q [N]	N_{f1}	N_{f2}
4	4217	110	1543	1110,174	1117,513
7	4217	150	971	678,676	634,259
8	5429	150	971	707,514	631,491
9	3006	150	1543	275,417	198,884
13	4217	150	2113	166,088	201,105
15	3006	175	971	364,153	366,164
18	3006	175	1543	164,835	163,474
19	4217	175	1543	169,382	164,384
20	5429	175	1543	228,379	231,132
22	4217	175	2113	121,642	127,770

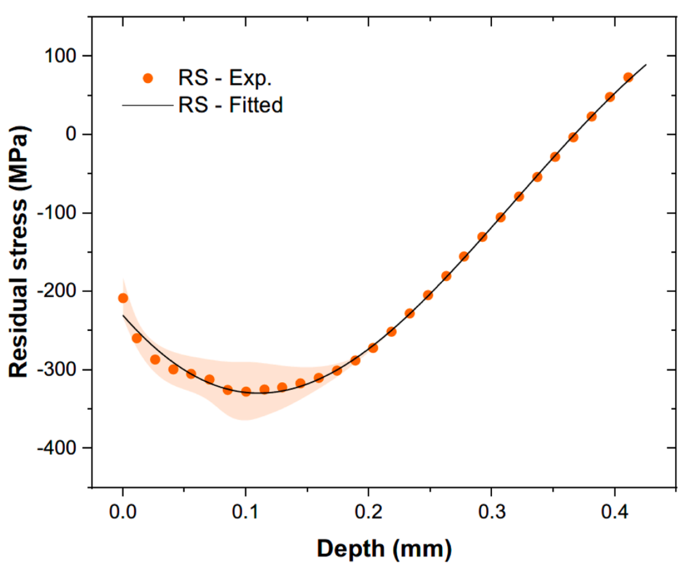

Fig. 2. Distribution of experimental and curve-fitted RS fields throughout depth.

ensure the reliability of the experimental results, each fatigue experiment was repeated twice, with the fatigue lifetime recorded as N_{f1} and N_{f2}, respectively. The average of these two values is then used for subsequent comparisons.

3. Theoretical background

3.1. Crack initiation

3.1.1. Critical plane method

The critical plane method refers to a plane with maximum value of the damage parameter. In this study, the Findley parameter (FP) is used as the damage parameter to analyse fretting fatigue behaviour, a widely recognized and commonly applied approach [37]. Findley relates the damage parameter to the shear stress and normal stress states as follows:

$$FP = \frac{\Delta\tau_{\max}}{2} + k_1\sigma_n^{\max} \tag{1}$$

where $\Delta\tau_{\max}$ represents the shear stress amplitude, ${\sigma_n}^{\max}$ is the maximum value of normal stress, and k_1 is a material-specific constant. k_1 can be determined using the following equation:

$$\frac{\sigma_{f-1}}{\tau_{f-1}} = \frac{2}{1 + \frac{k_1}{\sqrt{1+k_1^2}}} \tag{2}$$

where σ_{f-1}/τ_{f-1} denotes the ratio of fatigue limit in tension and torsion. In this study, the fatigue limits of Al 7075-T651 alloy are defined as pseudo-fatigue limits corresponding to 10^7 cycles. The value of σ_{f-1} and τ_{f-1} are 193 MPa and 117 MPa, respectively [18]. Therefore, k_1 is determined to be approximately 0.217.

To predict the crack initiation location (X_i), orientation (θ_i), and lifetime (N_i) using FP based on the critical plane method, it is crucial to analyse the stress history throughout the entire fretting fatigue cycle. Based on Eq. (1), FP depends on both the peak-to-peak amplitude of shear stress and the maximum normal stress, requiring a comprehensive collection of stress data throughout the fretting fatigue process. Mohr's circle transformation is used to convert the stresses on rotated planes, allowing the extraction of the necessary stress parameters for the analysis:

$$\sigma_n = \frac{1}{2}(\sigma_x + \sigma_y) + \frac{1}{2}(\sigma_x - \sigma_y)\cos(2\theta) + \tau_{xy}\sin(2\theta) \tag{3}$$

$$\tau_n = -\frac{1}{2}(\sigma_x - \sigma_y)\sin(2\theta) + \tau_{xy}\cos(2\theta) \tag{4}$$

3.1.2. The theory of critical distance

The critical plane method predicts the location, direction, and angle of crack initiation by analysing the critical surface at the point of peak stress. However, relying exclusively on this "hot spot" approach often leads to an underestimation of fatigue life. This is because stress concentrations at the peak point in fretting conditions cause damage parameters to decrease sharply with depth, leading to conservative predictions of fatigue initiation parameters. To improve accuracy, it is essential to represent damage parameters comprehensively in the critical area.

To address this limitation, various methods beyond the traditional hot spot approach can be employed, such as the line, volume, and quadrant methods. As shown in Fig. 3, the quadrant averaging method was used in this study. In this method, FP is averaged over a semi-circular zone, with the peak of the zone considered the node for generating the maximum FP. The zone is divided into left and right quadrants, and FP is calculated separately for each quadrant. By comparing the average values, the direction for the critical plane search is determined as follows: a) if the left quadrant's average FP is higher, the search spans from $-90°$ to $0°$ and b) if the right quadrant's FP is higher, the search spans from $0°$ to $90°$. This method combines the critical plane approach with the theory of critical distance (TCD) to predict crack initiation behaviour more accurately.

To implement this method, a Python script was developed for post-processing within ABAQUS®. The script extracts stress data from all nodes, covering an angular range from $-90°$ to $90°$ in $1°$ increments, ensuring that all potential crack initiation directions at each node are considered. Using this stress data, FP is calculated for the entire loading cycle at each node in all possible directions. The crack initiation location is identified at the point where FP is maximized, and the corresponding angle at that location determines the crack initiation orientation. The maximum FP value not only identifies the crack initiation site but also aids in estimating the crack initiation lifetime. The critical plane's maximum damage parameter across all points and planes provides a prediction for both the position and direction of crack initiation.

The critical distance (l_c), defined as the semicircle radius in the quadrant averaging method, which is crucial in obtaining the average FP value. Susmel and Taylor assumed a power function to describe the relationship between l_c and crack initiation lifetime (N_i) [38]:

$$l_c = AN_i^B \tag{5}$$

The parameters A and B can be determined by fitting two extreme cases. First, El Haddad proposed an empirical formula to calculate l_c [39]:

$$l_c = \frac{1}{\pi}\left(\frac{\Delta K_{\mathrm{th}}}{\sigma_{0[10^6]}}\right)^2 \tag{6}$$

where ΔK_{th} is the long crack threshold range of SIF, and $\sigma_{0[10^6]}$ corresponds to the plain fatigue strength at 10^6 cycles. Another formula, based on static failure, is given by [40]:

$$l_c = \frac{1}{\pi}\left(\frac{K_{IC}}{\sigma_{\mathrm{ref}}}\right)^2 \tag{7}$$

where σ_{ref} is the reference material strength, and K_{IC} is the plane strain material toughness, correlating static failure with a crack initiation lifetime of a single cycle. Eq. (6) and Eq. (7) provide l_c values for initiation lifetimes of 10^6 and 1 cycle, respectively. For SP-treated specimen, l_c is estimated to be around 80 μm, corresponding to a fatigue life of 1.35 $\times$ 10^6 cycles [41].

Once l_c is determined, the crack initiation lifetime (N_i) can be predicted using Park's equation [42]:

$$FP = \tau_f'(2N_i)^b \tag{8}$$

where τ_f' is the shear fatigue strength coefficient, having a value of 797 MPa, and b is the fatigue strength exponent in torsion, with a value of -0.126 [35].

3.2. Multiscale analysis

According to experimental observations, surface roughness enhances fretting fatigue life by dividing the contact interface into smaller localized zones and expanding the overall contact area radius compared to the theoretical radius for smooth surfaces [41]. At the microscale, rough surface contacts produce highly fluctuating pressure distributions due to asperity interactions. However, directly incorporating these microscales contact behaviours into macroscale simulations is computationally prohibitive. To address this, a kernel smoothing technique is applied to filter out high-frequency asperity-induced stress fluctuations while preserving essential macroscale trends, such as stress redistribution. To bridge the effects of microscale roughness with macroscale fatigue predictions, a multiscale analysis framework is employed to transfer the key features of the microscale contact response to the macroscale model. The flowchart of multiscale analysis is summarized in Fig. 4, which demonstrates how microscale features are obtained and upscaled to the macroscale model.

Firstly, a microscopic contact model based on the rough surface and the cylindrical pad is illustrated in Fig. 5(a). For 2D configuration, a normal load (P/L) is applied on the top of a cylinder having a radius R_0. The microscopic model allows contact analysis to provide insight into

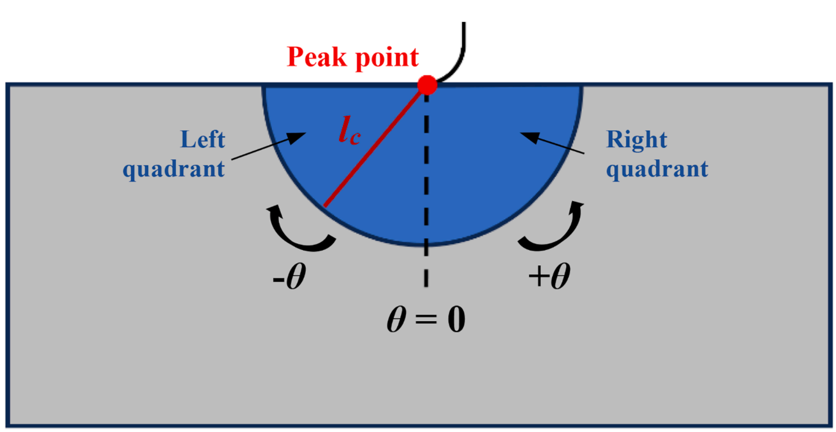

Fig. 3. Diagram of quadrant averaging method.

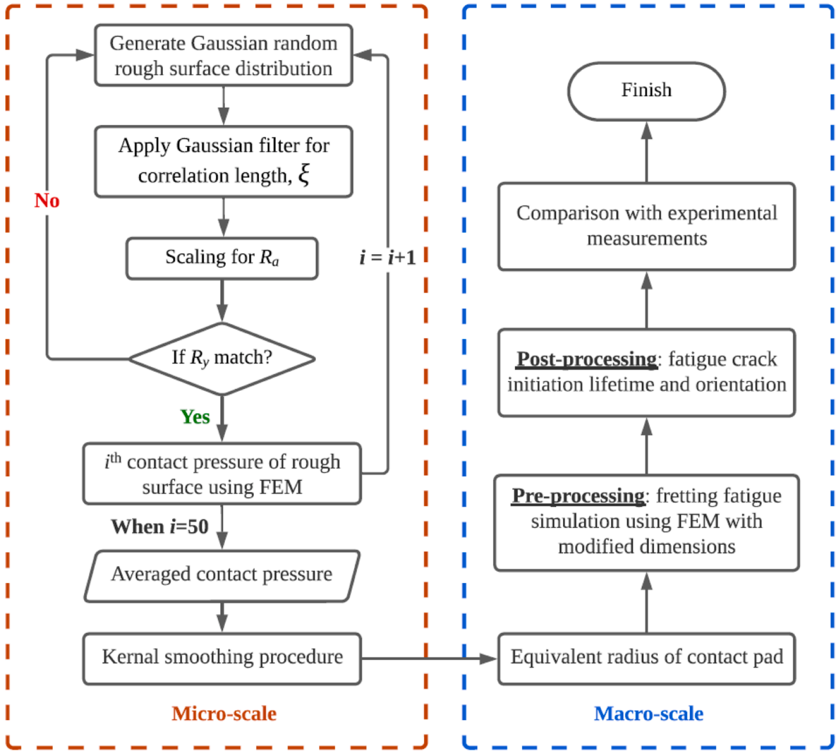

Fig. 4. Flowchart of multiscale analysis, including roughness generation and fretting fatigue simulation using FEM.

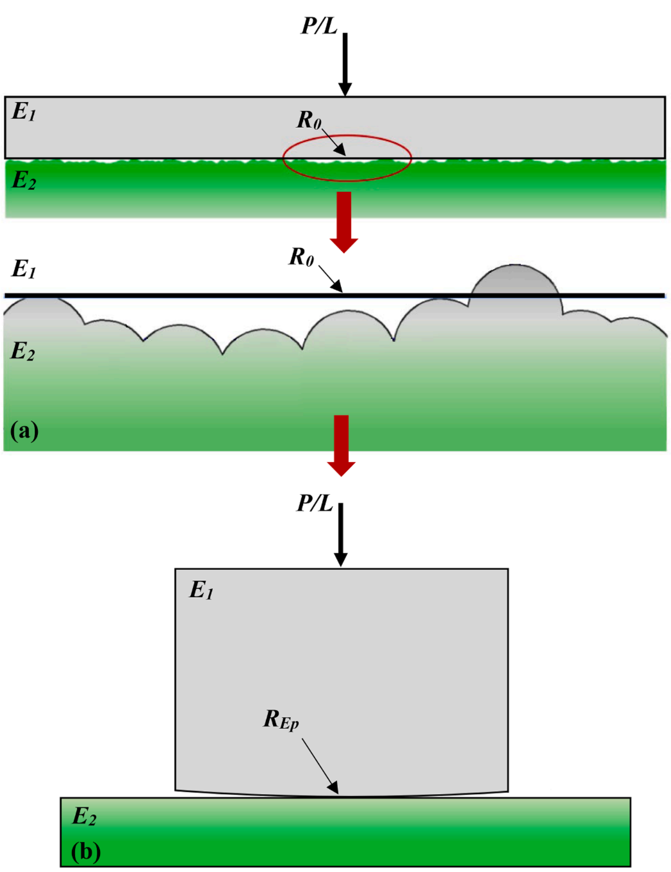

Fig. 5. Contact schematic of (a) micro- and (b) macro-scale models.

the microscopic contact behaviour. However, the contact pressure profile on rough surfaces exhibits significant fluctuations, making it challenging to extract key features [30]. To address this, a nonparametric technique known as kernel smoothing is applied to approximate the underlying smooth function from the observed data points. Kernel smoothing works by convolving the data with a kernel function, which is a smooth, symmetric function with a total area of one, helping capture the essential characteristics of the contact stress profile.

Nadaraya and Watson introduced the concept of an estimator based on locally weighted averages, employing a kernel function for weighting [43]. The Nadaraya–Watson estimator at a point x_0 is calculated as:

$$\hat{f}(x_0) = \frac{\sum_{i=1}^{n} K_w(x_0 - x_i) Y_i}{\sum_{i=1}^{n} K_w(x_0 - x_i)}, \quad \text{where } K_w(u) = \frac{1}{w} K\left(\frac{u}{w}\right) \tag{9}$$

where x_i represents the independent variables (observed design points) in the dataset, and Y_i corresponds to the dependent variables (the values being estimated). n is the total number of observations, and $K_w(u)$ is the kernel function evaluated at $u = x_0 - x_i$. Notably, K_w is a non-negative, symmetric function that integrates to 1. w is the bandwidth parameter, which controls the scale of smoothing.

Gaussian kernel is used because it provides a smooth and continuous weight distribution. Its properties, such as symmetry and rapid decay, make it well-suited capturing localized effects while avoiding discontinuities, which is essential for producing physically meaningful contact pressure distributions. w controls the level of smoothing. A smaller w preserves fine surface details, while a larger w leads to a more generalized, smoothed profile. Our objective is to obtain a contact pressure distribution that is both smooth and symmetric. Symmetry is especially desirable in this study because it simplifies the interpretation of stress distribution and allows for a more balanced replication of contact behaviour at the macroscopic scale. This is consistent with our multiscale approach, where the key features of microscale contact (e.g., peak contact pressure) must be retained while ensuring compatibility with smoother, macroscale contact geometries A larger w potentially overlooking significant features of the function (increasing bias), whereas a smaller w results in a more detailed but noise-sensitive estimate (increasing variance). To smooth the contact pressure data derived from the FEM, kernel smoothing was applied using MATLAB® code.

The microscale model can then be scaled up to develop a macroscopic model for computational efficiency if the key contact behaviour parameters are kept consistent with the microscopic behaviour. A one-directional strategy is adopted, where the microscopic model is analysed separately from the macroscopic model. This method allows the features extracted from the microscale, such as contact stress field, to serve as an input for the macroscale model. Therefore, the impact of surface roughness can be effectively scaled up from micro to macro. The contact pressure profile produced by FEM is averaged across tens of rough surfaces, with more details on the averaging process discussed in Section 5.2.

As shown in Fig. 5(b), by adjusting the radius of the cylindrical pad in the macroscale model, the contact pressure distribution closely replicates that of the microscale model, accounting for surface roughness. The equivalent radius (R_{Ep}) of macroscopic model is crucial for matching the microscale analysis. This approach ensures that the contact pressure distribution of the macroscopic model aligns with microscopic insights, providing a more accurate representation of the physical contact phenomena. R_{Ep} can be derived by comparing the Hertzian solution from the macroscale model with the contact pressure obtained from the microscale model [44]:

$$\begin{aligned} R_{Ep} &= \frac{PE^*}{\pi L p_{\max}^2}, \\ \frac{1}{E^*} &= \frac{1-\nu_1^2}{E_1} + \frac{1-\nu_2^2}{E_2} \end{aligned} \tag{10}$$

where E^* represents the equivalent elastic modulus, combining the elastic properties of both materials in contact, and $p_{\max}$ is the maximum value of contact pressure at microscale. Specifically, E_1 and E_2 are the elastic moduli, and ν_1 and ν_2 are the Poisson's ratios associated with the contact cylinder and the specimen, respectively. L denotes the contact length between the cylindrical pad and the planar specimen. For cylinder-on-plane configuration, whether micro- or macro scale model, half contact width (B_H) is determined as the distance from the edge of the contact area to the midpoint:

$$\begin{aligned} B_H &= \sqrt{\frac{4PR^*}{\pi E^* L}}, \\ \frac{1}{R^*} &= \frac{1}{R_1} + \frac{1}{R_2} \end{aligned} \tag{11}$$

where R^* is the effective radius of curvature of the two contact bodies. R_1 and R_2 are the elastic moduli associated of the cylinder and the specimen, respectively.

4. Numerical models

4.1. Surface roughness generation

Greenwood and Williamson describe the initial rough surface as an assembly of spherical asperities with uniform end radii, whose heights h follow a Gaussian statistical distribution [45]:

$$h(x) = \frac{1}{\sqrt{2\pi}} e^{-x^2/2} \tag{12}$$

A key metric for assessing surface topography is the characterization parameter [46]. The most used roughness parameter, R_a, is the arithmetic average of the absolute values of height deviations from the mean line within the evaluation length:

$$R_a = \frac{1}{l}\int_0^l |h(x)| dx \tag{13}$$

where l is the pre-set sampling length.

Another important parameter, R_y, represents the maximum peak-to-valley height, reflecting the vertical distance between the highest peak and the lowest valley within the surface profile:

$$R_y = h_{\max} - h_{\min} \tag{14}$$

where $h_{\max}$ and $h_{\min}$ are the highest (peak) and lowest (valley) point on the surface profile, respectively.

Additionally, ξ is defined as the distance at which the autocorrelation function drops to 10 % of its original value, measuring the extent to which surface features are correlated over distance. To simulate the impact of SP on surface roughness, ξ can be approximated based on the Almen intensity (A), as follows [47]:

$$\xi[\mu\text{m}] \approx 157 - \frac{122}{1+0.39A} \tag{15}$$

Given that the SP treatment is denoted as 9A-230H-90°, with $A = 9$, ξ calculates to approximately 129.9 μm, as described for the SP-treated specimen in Table 1. This calculated value of ξ aligns with the observed trend relative to Almen intensity, underscoring the reliability of Eq. (15) [48].

Specifically, rough surfaces with varying ξ are illustrated in Fig. 6, demonstrating how different correlation lengths significantly affect roughness profiles. It can be observed that surfaces with lower ξ exhibit more rapid changes, indicating that higher Almen intensities in SP processes tend to produce a smoother and more controlled surface modification, reflected in larger ξ values.

4.2. Introducing RS into FE model

In addition to the increased surface roughness, the SP-treated material exhibits a higher degree of compressive RS near the surface. Given the significant influence of RS on fatigue life, it is incorporated into the analysis of SP-treated samples. SP-induced RS can be considered as distribution of initial stress within the specimen for subsequent fretting fatigue simulation. To achieve this, SIGINI subroutine is employed to introduce an initial stress distribution equivalent to the measured RS, so that RS is directly incorporated into the FE model. The SIGINI subroutine is used to define the initial stress component along the x-axis (σ_{xx}) at each element's Gaussian integration points. This initialization occurs before the application of external loads and displacements, following the Lagrangian description.

To ensure that the experimental RS data are seamlessly integrated into the FE model, the discrete data points are processed using nonlinear curve fitting techniques to generate smooth RS distribution. Specifically, the RS profile of the SP-treated sample is represented by the following serpentine curve:

$$\begin{aligned} \sigma_{xx}(y) = 380.0405e^{1.16786y}\cos(-6.79525y + 27.35474), \\ \text{where} \quad -0.425 \le y \le 0 \end{aligned} \tag{16}$$

The fitted curve of Eq. (16) is added in Fig. 2, which is highly consistent with the experimental data. The contour corresponding to this curve is reflected in the FE model through the SIGINI subroutine, as shown in Fig. 7.

4.3. Multiscale analysis

4.3.1. Microscale FE model

The framework assumes homogeneous material response and excludes some other SP-induced microstructural changes, such as grain refinement or dislocation density. Fig. 4 illustrates the methodology for numerically generating a rough surface profile influenced by SP. All SP-modified roughness parameters (R_a, ξ, and R_y) are integrated in MATLAB® code. The process initiates by creating a rough surface profile along the x-axis using a Gaussian random distribution. Subsequently, a

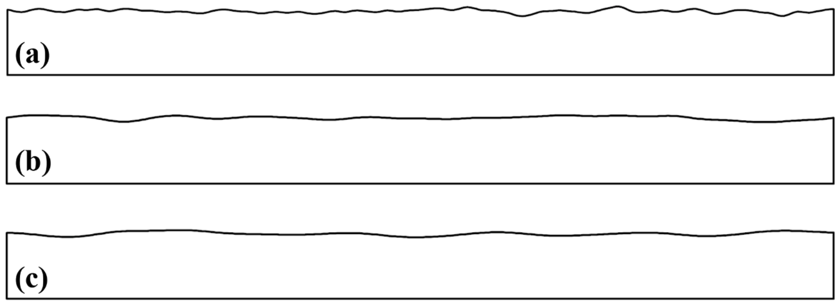

Fig. 6. Schematic diagram of numerically simulated rough contours considering different correlation lengths: (a) $\xi = 50$ μm, (b) $\xi = 139.9$ μm and (c) $\xi = 200$ μm.

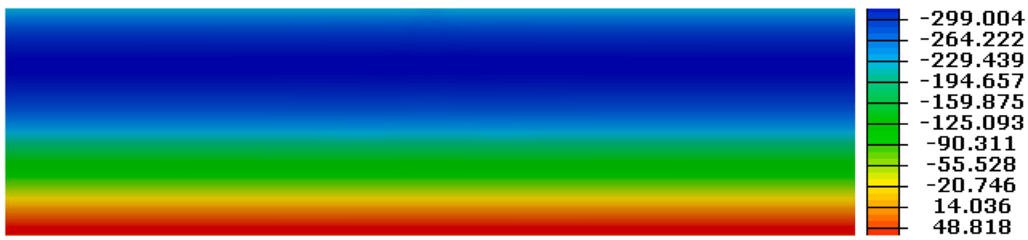

Fig. 7. RS [MPa] contours of the SP-treated FE model.

Gaussian filter is applied to this initial profile, tailored to the specified correlation length (ξ), refining the roughness pattern and appearance. The profile's overall height is then scaled to achieve the target average roughness (R_a). Finally, the profile's height is adjusted further to match the specified maximum peak-to-valley height (R_y), ensuring the surface does not exceed the designated maximum height difference and aligns with the desired roughness characteristics. The introduction of surface roughness alters CoF in the tangential direction, as detailed in Table 1. In line with the multiscale method discussed in Section 3.2, the effect of roughness in the normal direction is primarily considered through its influence on contact pressure distribution at the interface. To accurately evaluate the impact of roughness, a microscale model with a rough surface is developed, capturing the entire contact area within a small segment. Due to the symmetrical nature of the samples, the loading condition, and the testing procedure, the contact problem is simplified into a 2D model. Fig. 8 illustrates the construction of a cylindrical-on-plane configuration in ABAQUS®/Standard mode, simulating the contact behaviour between the surfaces. To achieve contact in the FE model, a concentrated force is strategically applied at a reference point (RP), which is connected to the top surface nodes of the cylinder via a multi-point constraint (MPC). This method ensures the force is evenly distributed across the linked nodes, preventing excessive deformation or distortion of the mesh.

In this model, both the contact pads and planar specimens are made from Al 7075-T651 alloy, with an elastic modulus of 71 GPa and a Poisson's ratio of 0.33. The pad radius (R_0) is set at 100 mm, while the plane's dimensions (length × height) are 3 × 0.25 mm^2. Notably, in incomplete contact problem, geometry and boundary conditions can affect contact behaviour. A sensitivity analysis on model height confirmed that heights $\geq$ 0.25 mm produce converged contact pressure distributions. Smaller heights tend to exaggerate stress gradients, while larger heights increase computational cost without significant improvement in accuracy.

The model is divided into two zones, i.e. the contact and non-contact areas. In the contact area, where surface roughness is most pronounced, the planar specimen is meshed with a fine grid of approximately 5 μm × 5 μm. The mesh size for the pad's contact area is slightly larger, at 10 μm × 10 μm. All contact surfaces on both the pad and the specimen are modelled using four-node plane strain elements (CPE4) to accurately simulate the contact behaviour. For regions away from the contact interface, a coarser mesh ranging from 5 to 80 μm is applied to reduce the total number of elements, thereby improving computational efficiency. These non-contact sections are modelled with four-node elements with reduced integration (CPE4R), further minimizing computational demands while maintaining accuracy in less critical areas.

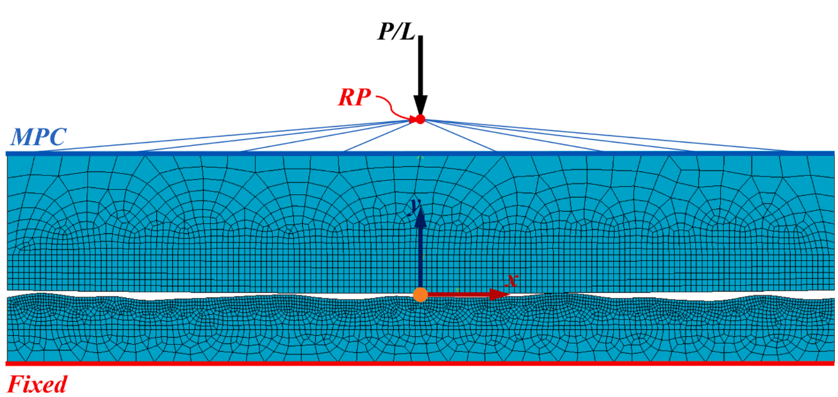

Fig. 8. Microscale contact FE model with rough surface.

The interaction between the deformable pad and the planar specimen is simulated using a surface-to-surface contact algorithm, which identifies contact pairs and accurately accounts for the contours of both contacting surfaces. This approach is particularly important for modelling rough surfaces, where significant variations in surface topography occur. The surface-to-surface algorithm prevents penetration more effectively than node-to-surface contact models, resulting in a more uniform distribution of contact pressure. Additionally, a hard contact algorithm is employed to further reduce penetration in the normal direction during simulations, enhancing the realism of the contact behaviour. In this setup, the rough surface of the specimen is designated as the slave surface, while the bottom surface of the pad is defined as the master surface. This arrangement ensures accurate modelling of the contact interaction, especially for surfaces with significant roughness.

4.3.2. Macroscale FE model

Considering the symmetry of the experimental setup, the macroscopic model for the fretting fatigue test is refined and illustrated in Fig. 9. The planar specimen has dimensions of 40 mm in length and 5 mm in width. R_{Ep} is critical for each cylinder-on-plane configuration, is determined through multiscale analysis. The methodology for calculating R_{Ep} is outlined in Section 3.2, with specific values for various cylinder-on-plane combinations provided in Section 5.3. The material for the model is Al 7075-T651 alloy, characterized by an elastic modulus of 71 GPa and a Poisson's ratio of 0.33. It is worth noting that plastic deformation and strain-hardening behaviour may further redistribute stress and alter crack initiation behaviour. However, to simplify the problem and reduce computational cost, the effect of surface roughness on the elastic stress gradient is considered in this study.

A symmetry boundary condition is applied to the bottom side of the specimen, constraining displacement along the y-axis ($U_2 = U_{R3} = 0$) and preventing rotation. The left and right sides of the pad are fixed in the x-direction, with rotational constraints ($U_1 = U_{R3} = 0$) are also applied. To accurately simulate fretting fatigue, a finite sliding formulation is used, allowing relative tangential displacements while accounting for friction. The hard contact model is specified for normal directional contact behaviour, and the Lagrange multiplier method is employed to handle tangential interactions effectively. In line with the contact modelling strategy, the bottom surface of the pad is designated as the master surface, while the top surface of the specimen is identified as the slave surface. This ensures precise simulation of the contact behaviour between the pad and specimen, particularly for capturing the fretting fatigue features.

Upon completing the FE model setup, the simulation process of fretting fatigue is segmented into following stages:

- **Initial Step: Incorporating RS.** The RS is introduced into the FE model in the initial step of simulation.
- **Step 1: Applying Normal Load.** Normal loads, as detailed in Table 2, are exposed on the pad's top surface during the loading stage. These loads are applied in the y-direction at RP, which is connected to the pad's top surface through MPC, ensuring even distribution.
- **Step 2: Applying Axial and Reaction Stresses.** As axial stress is introduced to the specimen's right-hand side, a counteracting reaction stress is applied on the left side to maintain equilibrium in the x-direction. The reaction stress is calculated based on the shear stress equation:

$$\sigma_{\text{reaction}} = \sigma_{\text{axial}} - \frac{Q}{A_h} \tag{17}$$

where A_h is the half-sectional area of the planar specimen, which amount to 40 mm^2.

- **Step 3: Reversing Axial and Reaction Loads.** Given that the axial stress ratio is set to -1, the reaction stress follows a harmonic pattern, remaining in phase. At this stage, the directions of both axial stresses and reaction forces are inverted to align with the testing procedure.

5. Results and discussion

5.1. Mesh sensitivity analysis

Since the Hertzian's analytical solution is available for smooth contact surfaces (i.e., without roughness) [49], a mesh sensitivity analysis was performed on the micromodel with two smooth profiles. This analysis, detailed in Section 4.3.1, followed the method used for generating microscopic model coordinates, setting the roughness parameters R_a and ξ to zero, which inherently results in R_y being zero as well. As a result, smooth surface conditions were established for both the cylindrical pad and the planar sample. To balance accuracy and computational efficiency in FE simulations, different mesh sizes of 2 μm, 5 μm, and 10 μm in the contact area are tested.

The variations in maximum contact pressure with mesh density under three different P's are shown in Fig. 10(a). These results are compared with Hertzian theoretical solutions, which predict maximum contact pressures of 218.3 MPa, 258.5 MPa, and 293.4 MPa for $P = 3006$ N, 4217 N, and 5429 N, respectively. The microscale FE model closely matches the analytical predictions, with a maximum discrepancy of <

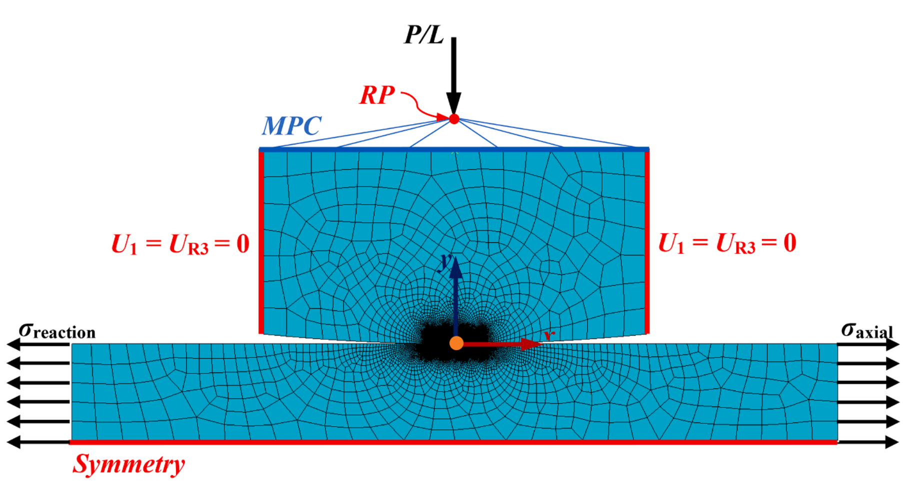

Fig. 9. Macroscale fretting fatigue FE model.

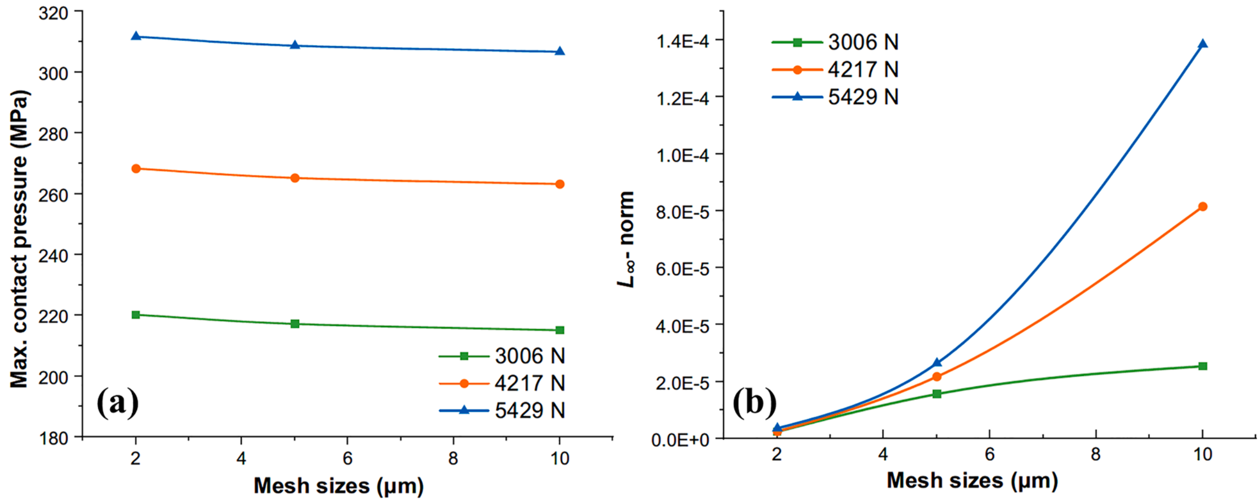

Fig. 10. (a) Maximum contact pressure and (b) infinite norm (L_∞) with different mesh sizes for different *P's*.

6.3 %. This strong alignment demonstrates the suitability of the chosen mesh sizes, loading, and boundary conditions for the microscale analysis. The simulation results using FEM also show that increasing mesh density slightly reduced the maximum contact pressure, indicating convergence. Further mesh refinement would result in minimal changes, confirming the suitability of the selected mesh size.

Fig. 10(b) illustrates the relationship between the infinite norm (L_∞) and mesh size for different *P's*. L_∞, defined as the maximum residual force ($r_{\max}$) across all elements in the final converged iteration of the last increment, shows that smaller mesh sizes result in lower errors. As mesh size increases, L_∞ also rises, indicating that coarser meshes tend to yield less accurate numerical solutions. For instance, at $P = 5429$ N, the smallest mesh size (2 μm) yields the lowest error of 3.68×10^{-6}, while the largest mesh size (10 μm) exhibits significantly highest errors of 1.38×10^{-4}. This indicates the critical importance of using fine mesh sizes for achieving precise simulations, particularly under higher loads.

Although higher mesh densities improve result accuracy across various conditions, they also significantly increase computational demands. However, the error associated with a 5 μm mesh size remained relatively low (2.65×10^{-5}) compared to the larger increase observed with a 10 μm mesh. This suggests that a 5 μm mesh size offers a more favourable balance between accuracy and computational cost. Consequently, the 5 μm mesh size is considered optimal for subsequent simulations, as it provides an effective compromise between precision and efficiency.

5.2. *Effect of roughness on contact stress*

Following the mesh sensitivity analysis, the microscale model developed in this study effectively examines the influence of surface roughness on contact pressure distribution. Fig. 11 presents the contact pressures derived from tens of FE models, each featuring a unique rough surface profile induced by SP treatment. The pressure values and contact widths are normalized against the maximum Hertzian contact pressure ($p_{H,\max}$) and the half contact width (B_H), respectively. This normalization highlights the deviation of actual contact conditions from the

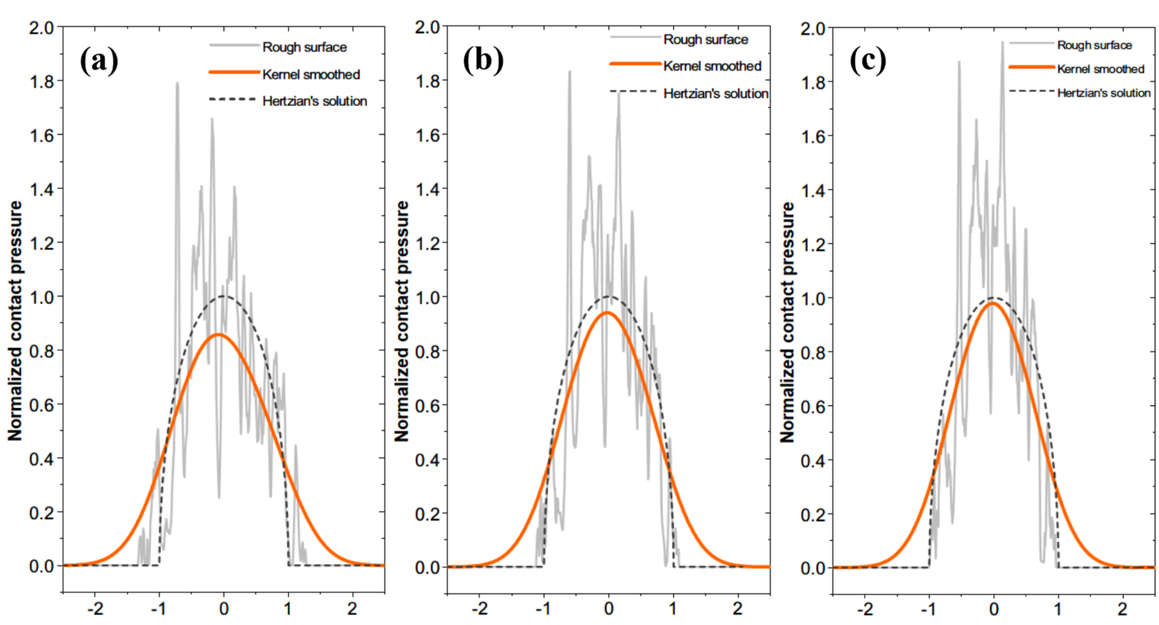

Fig. 11. Normalized Hertzian, rough surface and kernel smoothed contact pressure distributions for the microscale model for (a) $P = 3006$ N, (b) $P = 4217$ N and (c) $P = 5429$ N.

idealized Hertzian theory, caused by surface roughness and the smoothing effects of the regression applied to the rough profiles. However, there is no one-size-fits-all rule for w, different w is selected for different loading conditions: $w = 0.4$ for $P = 3006$ N, $w = 0.3$ for $P = 4217$ N, and $w = 0.25$ for $P = 5429$ N.

The maximum contact pressure obtained from kernel smoothing procedure is lower than the Hertzian solution under various loading conditions, which is consistent with the experimental measurements [41]. This is because the contact area can be split into multiple small areas by the asperities, and the contact pressure is concentrated in these local areas. The observed contact area radius is larger than the theoretical Hertzian radius of the smooth surface, resulting in a decrease in the maximum contact pressure.

A notable observation is that the impact of surface roughness on contact mechanics diminishes as P increases. When $P = 3006$ N, the normalized maximum contact pressure after kernel smoothing is 0.858. However, as P increases to 4217 N and 5429 N, the normalized contact pressure rises to 0.940 and 0.979, respectively. This trend is evident in the narrowing gap between the kernel-smoothed solutions, which account for surface roughness, and the idealized Hertzian theory, which assumes perfectly smooth surfaces, can be attributed to several factors. As P increases, the contact area expands, engaging more surface asperities in load distribution. This broader contact area helps to equalize the pressure across the asperities, reducing the influence of microscale roughness. Consequently, under higher loads, the macroscopic behavior begins to approach the Hertzian solution, which assumes smooth and continuous contact surfaces. Furthermore, at higher loads, more asperities bear the load, effectively approximating a smoother surface. This makes Hertzian assumptions more applicable in high-load scenarios compared to the discrete contact points that dominate at lower loads due to roughness. In essence, the trend suggests that the relative impact of surface roughness on maximum contact pressure decreases as the load increases.

To ensure consistency, the same set of rough surface profiles is used across all loading scenarios. As shown in Fig. 12, the selection of the number of roughness is evaluated by comparing the maximum contact pressure under different levels of averaging, focusing on the range from 30 to 50 averages. The maximum contact pressure accounting for roughness is normalized by the maximum contact pressure obtained from FEM without considering roughness. This normalization characterizes the extent to which roughness mitigates the peak of equivalent contact pressure. The analysis concluded that the maximum contact pressure values stabilized at 50 averages, especially at lower loads. This suggests that this average value is sufficient to capture the key features of the contact stress distribution affected by surface roughness. At this threshold, the kernel smoothing technique effectively balances noise reduction with data smoothing while preserving essential features of the pressure distribution. Thus, selecting 50 averages ensures a precise depiction of surface roughness's impact, confirming the effectiveness of this approach for accurately capturing the effects of roughness on contact pressure.

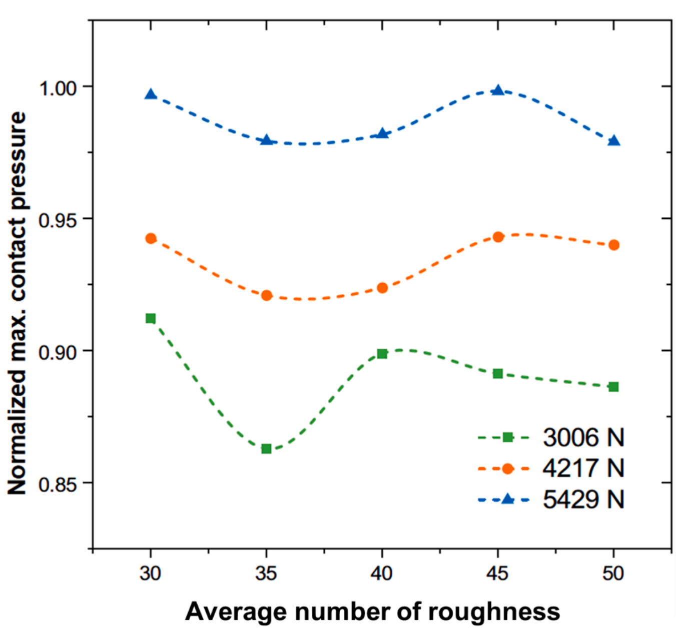

Fig. 12. Normalized maximum contact pressure versus the average number of roughness.

The observation of more pronounced fluctuations in contact pressure under lower P suggests that surface roughness has a more significant effect in this condition. This can be attributed to the smaller contact area at lower loads, where variations in surface topography have a greater impact on the distribution of contact pressures. Local peaks and valleys on the rough surface can cause higher stress concentrations, making the system more sensitive to the effects of roughness. As P increases, the contact area expands, allowing the load to be distributed over a larger surface. This broader distribution reduces the influence of localized surface irregularities, smoothing out the overall pressure distribution. Consequently, the fluctuations in contact pressure due to surface roughness become less noticeable, illustrating that the impact of roughness on contact pressure diminishes as the load increases.

At the end of **Step 2**, the maximum contact stress distributions are obtained. Fig. 13 compares the effect of roughness on contact pressure distribution under different loading conditions with and without roughness. It is worth noting that all FE models include RS because SP tends to cause roughness while introducing RS. Taking Fig. 13(a) as an example ($P = 4217$ N, and $\sigma_{\text{axial}} = 110$ MPa), the inclusion of roughness reduces the peak contact pressure and redistributes stresses over a wider contact area compared to simulations with RS alone. This stress redistribution aligns with the microscale trends observed in Fig. 11.

Similarly, Fig. 14 illustrate the shear stress distribution. It is evident that, regardless of the loading conditions, the presence of surface roughness consistently reduces the maximum stress values and redistributes the stresses over a larger contact area.

5.3. Effect of roughness on crack initiation

5.3.1. Crack initiation orientation and location

Based on Eq. (10) from the multi-scale analysis, the cylinder radius (R_0) in the FE model of the SP-treated specimen can be adjusted to R_{Ep}, incorporating the effects of surface roughness. R_{Ep} under various loading conditions is presented in Table 3.

As described in Section 3.1.1, the critical plane method is used in this study to examine crack initiation behaviour. The crack initiation location (X_i) is identified through the damage parameter FP, which corresponds to the peak point, as shown in Table 4. As shown in Eq. (11), B_H considers the material geometry, properties, and applied load. B_H increases with higher P, indicating a larger contact area. Since X_i is obtained from FEM, thus B_H should be also obtained from FEM to make them consistent to be compared. For the load scenarios presented in Table 2, three set of B_H for ignoring and considering roughness are observed: (1.199 mm, 1.299 mm), (1.349 mm, 1.449 mm) and (1.499 mm, 1.649 mm), corresponding to $P = 3006$ N, 4217 N, and 5429 N, respectively.

The ratio X_i/B_H is introduced here to evaluate relative position of crack initiation relative to the contact edge. Across all tests, $X_i/B_H < 1$ indicates crack initiation inside the half-contact width from the midpoint, typically at the trailing edge. This finding holds for both FE models with or without roughness, with rough models consistently exhibiting almost same X_i/B_H ratio.

Incorporating the quadrant averaging method with the critical plane method, the crack initiation angles can be explored in this study.

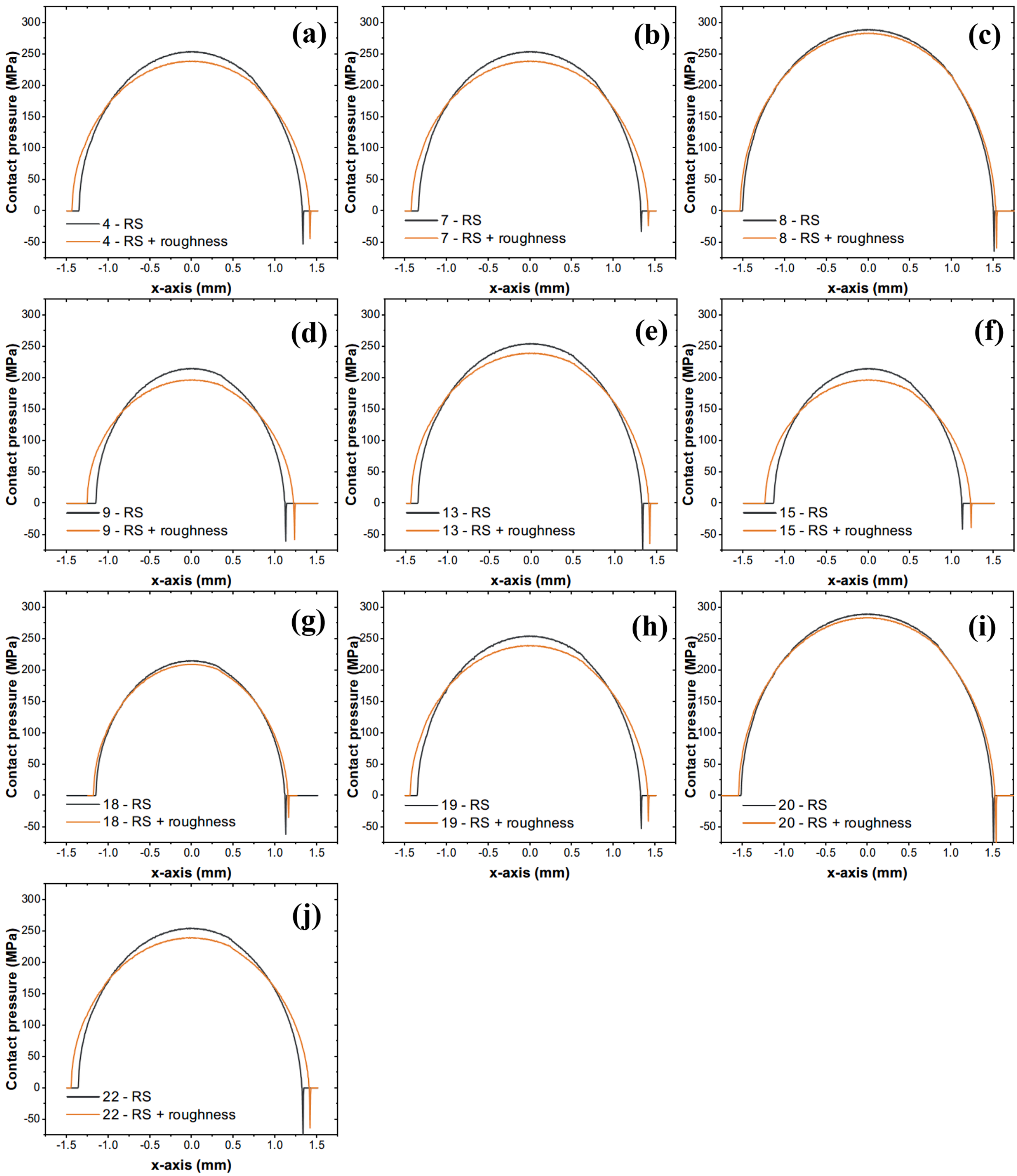

Fig. 13. Contact pressure distribution along *x*-axis for SP-treated specimens for different loading conditions: (a) Case 4, (b) Case 7, (c) Case 8, (d) Case 9, (e) Case 13, (f) Case 15, (g) Case 18, (h) Case 19, (i) Case 20 and (j) Case 22.

Dimensionless damage parameters, FP's, across all angles at the peak point are depicted in Fig. 15, showing minimal differences between curves that disregard and those that consider surface roughness. This observation suggests that surface roughness has a negligible impact on crack initiation orientation.

The crack initiation direction, identified by the regions with higher average damage parameters, is presented in Table 5 and expressed in negative degrees. This indicates that, across all tests, cracks tend to initiate in directions where the left quadrant exhibits higher average damage parameters than the right one, searching for the critical plane within angles from -90° to 0°. For samples with or without roughness, FE simulations show that the crack initiation directions range from -52° to -54°. This subtle difference indicates that surface roughness has a limited influence on crack initiation orientation, according to the

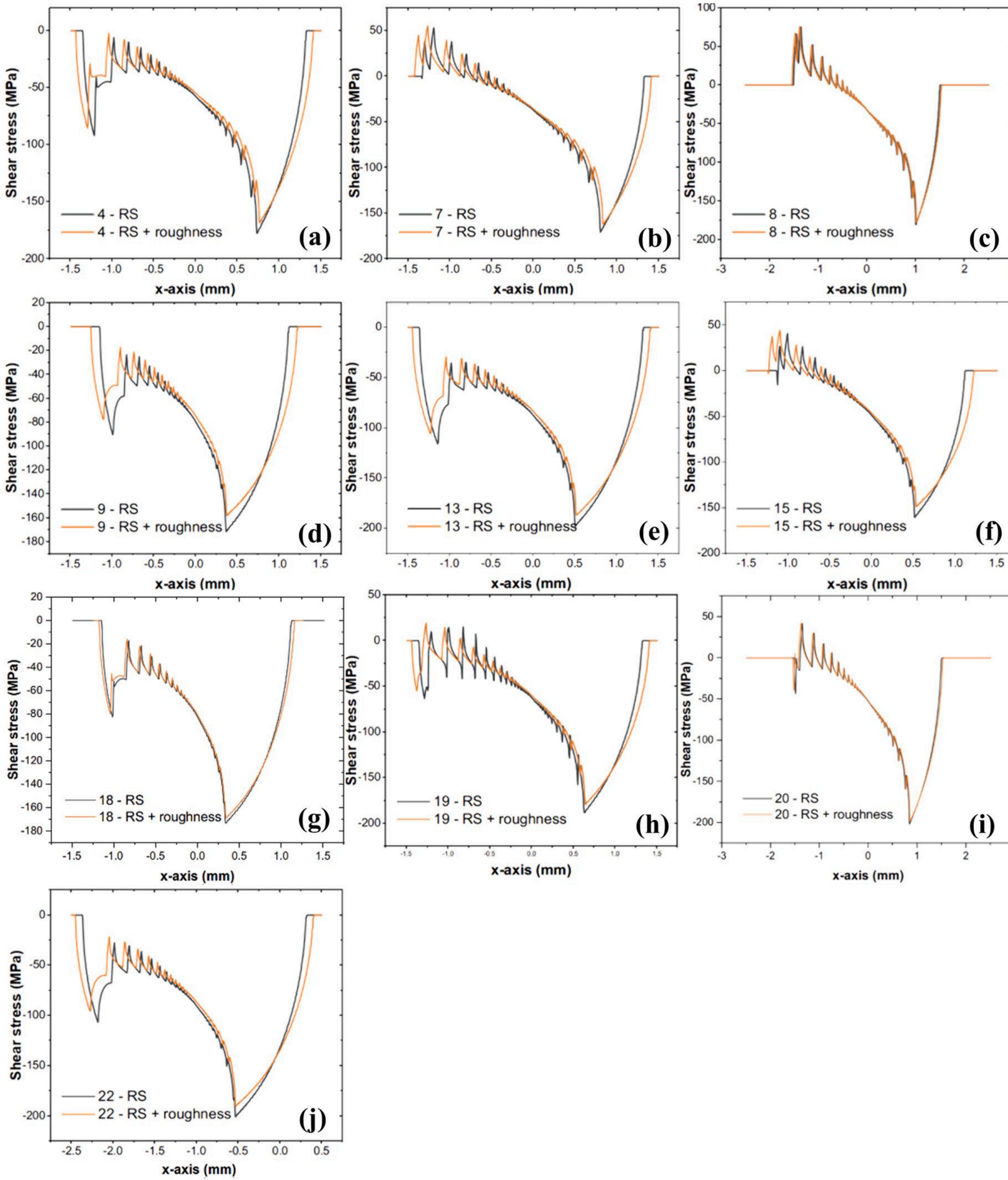

Fig. 14. Shear stress distribution along x-axis for SP-treated specimens for different loading conditions: (a) Case 4, (b) Case 7, (c) Case 8, (d) Case 9, (e) Case 13, (f) Case 15, (g) Case 18, (h) Case 19, (i) Case 20 and (j) Case 22.

numerical simulations under various loading conditions.

5.3.2. Crack initiation lifetime

The crack initiation lifespan under various loading scenarios is determined using the global maximum FP derived from FE post-processing, as stated in Eq. (8). For the SP-treated specimen, the crack initiation lifetime of the FE models with or without roughness is compared in Fig. 16(a). The findings indicate a notably longer crack initiation lifespan for tests accounting for roughness, highlighting SP-induced roughness's significant role in enhancing crack initiation durability.

To quantify roughness's impact on initiation lifetime as obtained by FEM, the following equation is used:

Table 3
Cylinder radii of smooth specimen and rough specimen used for fretting fatigue simulations.

P [N]	R_0 [mm]	R_{Ep} [mm]
3006	100	119.479
4217		113.163
5429		104.260

Table 4
Crack initiation location.

Test No.	X_i [mm]	B_H [mm]	X_i /B_H
4 - smooth	1.327	1.349	0.98
4 - rough	1.412	1.449	0.97
7 - smooth	1.339	1.349	0.99
7 - rough	1.414	1.449	0.98
8 - smooth	1.409	1.499	0.94
8 - rough	1.539	1.649	0.93
9 - smooth	1.121	1.199	0.93
9 - rough	1.227	1.299	0.94
13 - smooth	1.324	1.349	0.98
13 - rough	1.399	1.449	0.97
15 - smooth	1.124	1.299	0.87
15 - rough	1.228	1.409	0.87
18 - smooth	1.121	1.199	0.93
18 - rough	1.146	1.299	0.88
19 - smooth	1.326	1.349	0.98
19 - rough	1.411	1.449	0.97
20 - smooth	1.409	1.499	0.94
20 - rough	1.531	1.649	0.93
22 - smooth	1.324	1.349	0.98
22 - rough	1.399	1.449	0.97

$$\Delta_{N_i} = \frac{N_{i,\text{rough}} - N_{i,\text{smooth}}}{N_{i,\text{smooth}}} \times 100\% \tag{18}$$

Fig. 16(b) shows that a significant positive difference occurs in Test 4 with the lowest combined value of P and σ_{axial}, where the SP-induced roughness leads to a 43.2 % increase in crack initiation lifetime.

This trend continues, with the roughness improvements still being pronounced for Tests 4, 15, and 20, at 31.3 %, 28.7 % and 27.4 %, respectively. It indicates that the roughness consistently benefits lifetime extension, though the impact diminishes with increased loading condition. The underlying mechanism is that the surface roughness produced by SP creates peaks and valleys that concentrate stress at specific points while redistributing it over a larger area, as shown in Fig. 11(a). The introduction of roughness causes the contact area to split into many small regions, resulting in a more uniform stress distribution across the surface. This localized contact stress reduces the SIF compared to smooth surface contact, which in turn slows the accumulation of local damage that leads to crack initiation [41]. As a result, crack formation is delayed, positively impacting the fretting crack initiation lifespan.

At higher loads, such as in Test 8, the observed improvement decreases to just 2.17 %. This reduction is likely due to increased material deformation at higher loads, which further reduces the influence of microscopic surface roughness. As the surface peaks and valleys flatten, the initial high stress concentrations become more evenly distributed across the material. This diminishes the local protective effect of the surface roughness, resulting in a stress distribution at the microscopic level that more closely resembles to that of a smooth surface, as shown in Fig. 11(c). Consequently, at higher loads, the benefit of surface roughness for fatigue crack resistance is reduced because the changes in microscopic stress distribution are less pronounced compared to surfaces without roughness.

The impact of incorporating surface roughness on the prediction accuracy of fretting fatigue lifetime for SP-treated specimens remains uncertain. By comparing the predicted lifetimes of specimens, both ignoring and considering roughness, against experimental measurements, the effect of surface roughness on lifetime prediction accuracy can be evaluated. For SP-treated Al 7075-T651, observations based on the extended maximum tangential stress (EMTS) criterion indicate that crack propagation accounts for approximately 30 % of the total fatigue life [18]. Accordingly, 70 % of the total fatigue life measured experimentally is considered to represent the crack initiation phase. Fig. 17(a) compares the predicted total lifetimes with experimental outcomes, where all the predictions align within the ± 3 N error margin.

Both factors significantly enhance fatigue life, contributing to the underestimation observed in our predictions. Notably, all predicted values are below the experimental diagonal, regardless of roughness, indicating that the model tends to underestimate lifetime. This trend persists due to the deliberate exclusion of other SP-modified factors. Nonetheless, incorporating roughness into predictions yields results that align more closely with experimental data, highlights the potential accuracy benefits of considering surface roughness in lifespan estimations. Notably, the discrepancy between the experimental and FE results mainly stems from neglecting other factors induced by SP, such as the microscale properties of grains induced by SSPD [18].

Similarly, to quantify the errors in fretting fatigue lifetime predictions compared with experimental outcomes, the following formulas are employed:

$$\begin{aligned} error_{\text{smooth}} &= \frac{N_{f,\text{exp}} - N_{f,\text{smooth}}}{N_{f,\text{exp}}} \times 100\% \\ error_{\text{rough}} &= \frac{N_{f,\text{exp}} - N_{f,\text{rough}}}{N_{f,\text{exp}}} \times 100\% \end{aligned} \tag{19}$$

As shown in Fig. 17(b), the observed discrepancy between simulated and experimental results stems primarily from the inherent variability in the experimental data. As illustrated in Table 2, for instance, Test 9 exhibits a significantly lower σ_{axial}, and P compared to Test 20. However, their fatigue lifetime nearly identical. So, the large variance of approximately 38.5 % (especially N_{f2} for Test 9) directly leads to the high variability in fatigue life comparisons.

In the other tests, incorporating roughness into the model enhances the predicted fatigue life, thereby reducing the prediction error compared to the model that ignores roughness. Notably, Test 15 demonstrates the most significant improvement in prediction accuracy when roughness is accounted for, with the error decreasing from 27.7 % to 7.02 %. This test involved a lower load combination of P and σ_{axial}, highlighting a scenario where surface roughness plays a critical role in influencing fatigue life. The model that includes surface roughness provides predictions that align more closely with the experimental data, making the consideration of roughness essential for accurate fretting fatigue analysis of SP-treated samples.

In contrast, under higher loading conditions, such as in Tests 8 and 20, the prediction accuracy improves only marginally when considering roughness, by 2.17 % and 5.32 %, respectively. This trend suggests that at higher loading levels, the impact of surface roughness on fretting fatigue behaviour diminishes. Consequently, the difference in fatigue life between models that account for roughness and those that do not becomes smaller at higher loads. This observation indicates that under such conditions, the fatigue behaviour is primarily governed by the material's intrinsic properties and the applied load, reducing the relative influence of surface roughness on fatigue performance.

6. Conclusions

1) This study investigates the effect of surface roughness induced by SP on fretting fatigue properties, including crack initiation location, direction, and lifespan. Firstly, the effect of roughness on the contact pressure distribution in the microscopic model is simulated. This allows for the establishment of a macroscale FE model that incorporates the impact of roughness based on multi-scale analysis

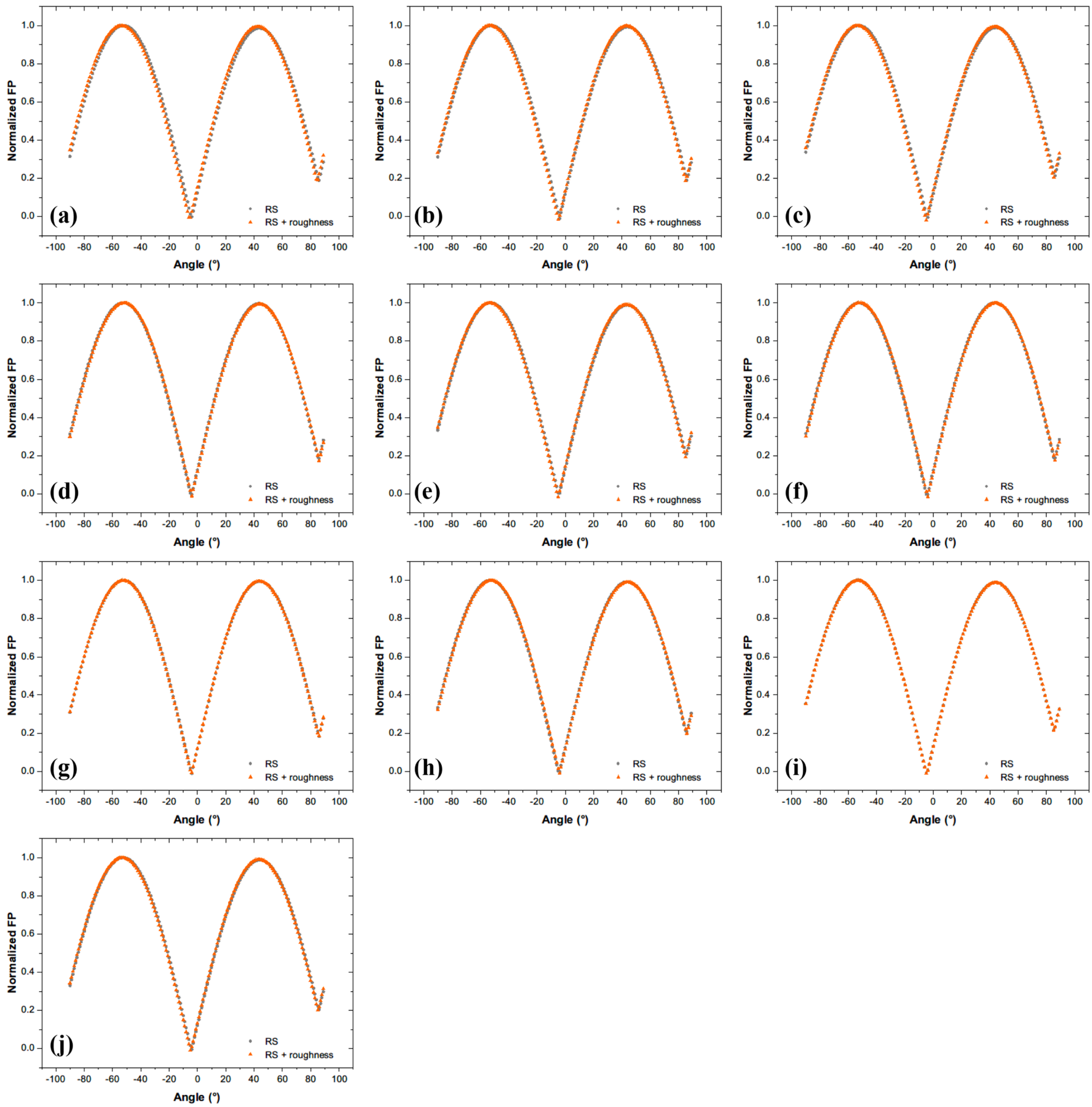

Fig. 15. Normalized damage parameters at the peak point as the angle changes.

Table 5
Crack initiation angles of smooth and rough specimens.

Test No.	θ_0 [°]	θ_{rough} [°]
4	−54	−52
7	−54	−53
8	−53	−54
9	−52	−52
13	−53	−53
15	−53	−52
18	−52	−52
19	−53	−52
20	−53	−53
22	−52	−53

approach. As a result, the fretting fatigue behaviour of SP-treated specimens, both with and without considering surface roughness, can be simulated to reveal how roughness affects fretting fatigue performance.

2) While surface roughness has minimal impact on the crack initiation angle and location, it markedly enhances the predicted fretting fatigue lifetime. For instance, under relatively lower normal load conditions such as in Test 9, surface roughness extends the total lifetime by 44.6 %. However, under higher normal load conditions, such as in Test 8, the improvement in crack initiation lifetime due to roughness is only 2.17 %, indicating that the benefits of roughness diminish as normal load increases.
3) Moreover, incorporating surface roughness into the FE model substantially enhances the prediction accuracy of fretting fatigue total

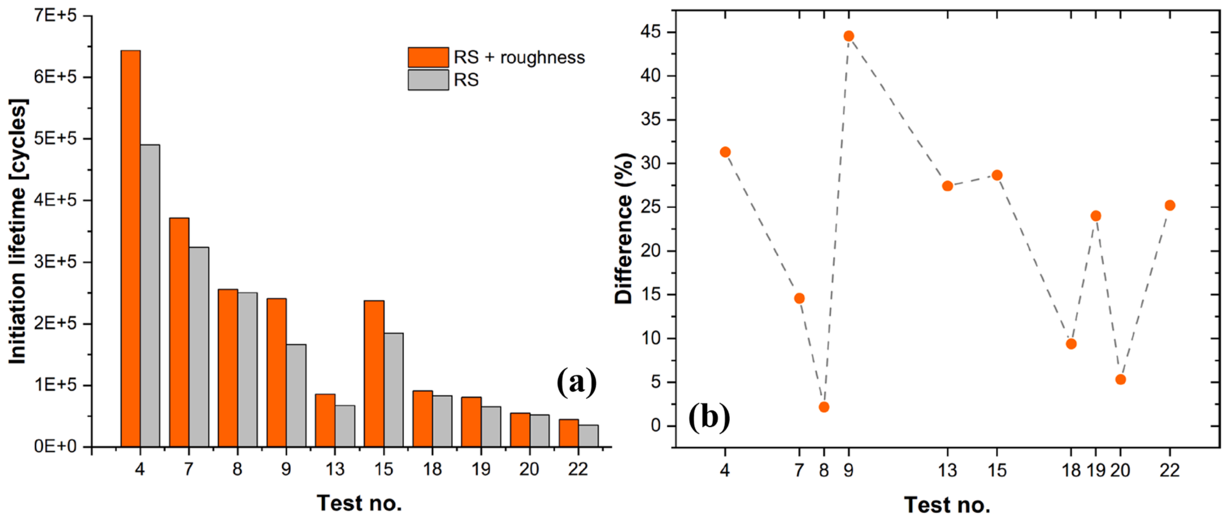

Fig. 16. Predicted crack initiation lifetimes considering or ignoring roughness of SP-treated specimens in terms of (a) bar graph and (b) percentage difference.

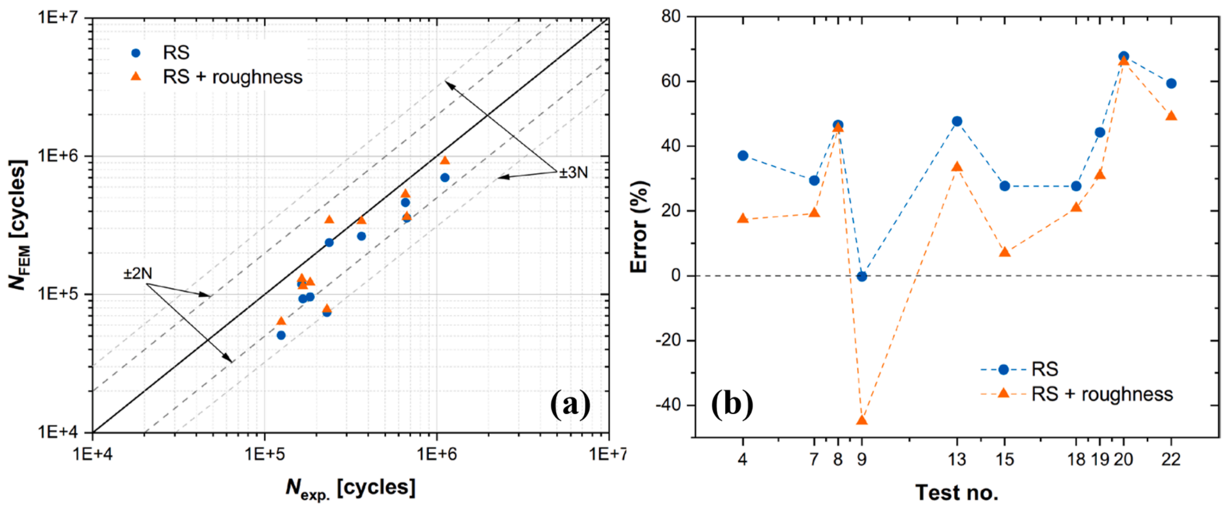

Fig. 17. (a) Comparison of FE predicted and experimental [19] total lifetime and (b) corresponding percentage error.

lifetime for SP-treated specimens. In lower load scenarios, such as Test 15, the prediction error is reduced from 27.7 % to 7.02 % compared to models that do not account for roughness. Even at higher loads, such as Test 8, the prediction error is slightly improved. These findings underscore the importance of accounting for surface roughness to accurately predict fretting fatigue behaviour in SP-treated specimens.

CRediT authorship contribution statement

Chao Li: Conceptualization, Formal analysis, Methodology, Writing – original draft. **Sutao Han:** Software, Validation. **Can Wang:** Methodology, Visualization. **Auezhan Amanov:** Supervision, Writing – review & editing. **Lihua Wang:** Supervision, Writing – review & editing. **Magd Abdel Wahab:** Writing – review & editing, Supervision, Investigation, Conceptualization.

Declaration of competing interest

The authors declare that they have no known competing financial interests or personal relationships that could have appeared to influence the work reported in this paper.

Acknowledgments

This work was supported and funded by the Chinese Scholarship Council (CSC). This work is supported by the National Natural Science Foundation of China (Project no. 12272270) and the Shanghai Pilot Program for Basic Research.

Data availability

Data will be made available on request.

References

[1] D. Nowell, D. Dini, D.A. Hills, Recent developments in the understanding of fretting fatigue, Eng. Fract. Mech. 73 (2006) 207–222, https://doi.org/10.1016/j.engfracmech.2005.01.013.

[2] S.L. Sunde, B. Haugen, F. Berto, Experimental and numerical fretting fatigue using a new test fixture, Int. J. Fatigue 143 (2021), https://doi.org/10.1016/j.ijfatigue.2020.106011.

[3] S. Sun, L. Li, K. He, Z. Yue, W. Yang, Z. Yu, Fretting fatigue damage mechanism of nickel-based single crystal superalloys at high temperature, Int. J. Mech. Sci. 186 (2020) 105894, https://doi.org/10.1016/j.ijmecsci.2020.105894.

[4] J. Wang, T. Chen, C. Zhou, Crystal plasticity modeling of fretting fatigue behavior of an aluminum alloy, Tribol. Int. 156 (2021) 106841, https://doi.org/10.1016/j.triboint.2020.106841.

[5] Z bing Cai, Z yang Li, M gui Yin, M hao Zhu, Z rong Zhou, A review of fretting study on nuclear power equipment, Tribol. Int. 144 (2020) 106095, https://doi.org/10.1016/j.triboint.2019.106095.
[6] N.A. Bhatti, M. Abdel Wahab, Fretting fatigue crack nucleation: a review, Tribol. Int. 121 (2018) 121–138, https://doi.org/10.1016/j.triboint.2018.01.029.
[7] S. Qutaba, M. Asmelash, K. Saptaji, A. Azhari, A Review on Peening Processes and its Effect on Surfaces, 120, Springer, London, 2022, https://doi.org/10.1007/s00170-022-09021-6.
[8] G.H. Majzoobi, F. Abbasi, On the effect of shot-peening on fretting fatigue of Al7075-T6 under cyclic normal contact loading, Surf. Coat. Technol. 328 (2017) 292–303, https://doi.org/10.1016/j.surfcoat.2017.08.067.
[9] C. Revilla-Gomez, J.Y. Buffiere, C. Verdu, C. Peyrac, L. Daflon, F. Lefebvre, Assessment of the surface hardening effects from hammer peening on high strength steel, Procedia Eng. 66 (2013) 150–160, https://doi.org/10.1016/j.proeng.2013.12.070.
[10] C. Li, A. Amanov, Y. Li, C. Wang, D. Wang, M. Abdel Wahab, Prediction of residual stress distribution induced by ultrasonic nanocrystalline surface modification using machine learning, Adv. Eng. Softw. 188 (2024) 103570, https://doi.org/10.1016/j.advengsoft.2023.103570.
[11] A. Amanov, R. Karimbaev, E. Maleki, O. Unal, Y.S. Pyun, T. Amanov, Effect of combined shot peening and ultrasonic nanocrystal surface modification processes on the fatigue performance of AISI 304, Surf. Coat. Technol. 358 (2019) 695–705, https://doi.org/10.1016/j.surfcoat.2018.11.100.
[12] Y. Zhang, F. Lai, S. Qu, V. Ji, H. Liu, X. Li, Effect of shot peening on residual stress distribution and tribological behaviors of 17Cr2Ni2MoVNb steel, Surf. Coat. Technol. 386 (2020) 125497, https://doi.org/10.1016/j.surfcoat.2020.125497.
[13] N.K.R. Naidu, S.G.S. Raman, Effect of shot blasting on plain fatigue and fretting fatigue behaviour of Al-Mg-Si alloy AA6061, Int. J. Fatigue 27 (2005) 323–331, https://doi.org/10.1016/j.ijfatigue.2004.07.007.
[14] A. Świetlicki, M. Szala, M. Walczak, Effects of shot peening and cavitation peening on properties of surface layer of metallic materials—A short review, Materials. (Basel) 15 (2022), https://doi.org/10.3390/ma15072476.
[15] A. Amanov, R. Karimbaev, C. Li, M.A. Wahab, Effect of surface modification technology on mechanical properties and dry fretting wear behavior of Inconel 718 alloy fabricated by laser powder-based direct energy deposition, Surf. Coat. Technol. 454 (2023) 129175, https://doi.org/10.1016/j.surfcoat.2022.129175.
[16] S. Vantadori, J.V. Valeo, A. Zanichelli, Fretting fatigue and shot peening: a multiaxial fatigue criterion including residual stress relaxation, Tribol. Int. 151 (2020), https://doi.org/10.1016/j.triboint.2020.106537.
[17] C. Li, A. Amanov, C. Wang, L. Wang, M. Abdel Wahab, Effect of laser shock peening on fretting wear behaviour of AISI 304 stainless alloy, Tribol. Int. 193 (2024) 109386, https://doi.org/10.1016/j.triboint.2024.109386.
[18] C. Wang, K. Fan, C. Li, M. Abdel Wahab, Prediction of the effect of shot peening residual stress on fretting fatigue behaviour, Int. J. Fatigue 176 (2023) 107909, https://doi.org/10.1016/j.ijfatigue.2023.107909.
[19] V. Martín, J. Vázquez, C. Navarro, J. Domínguez, Fretting-fatigue analysis of shot-peened Al 7075-T651 test specimens, Metals. (Basel) 9 (2019), https://doi.org/10.3390/met9050586.
[20] B.J. Foss, S. Gray, M.C. Hardy, S. Stekovic, D.S. McPhail, B.A. Shollock, Analysis of shot-peening and residual stress relaxation in the nickel-based superalloy RR1000, Acta Mater. 61 (2013) 2548–2559, https://doi.org/10.1016/j.actamat.2013.01.031.
[21] W.Z. Zhuang, G.R. Halford, Investigation of residual stress relaxation under cyclic load, Int. J. Fatigue 23 (2001) 31–37, https://doi.org/10.1016/s0142-1123(01)00132-3.
[22] M.A.S. Torres, H.J.C. Voorwald, An evaluation of shot peening, residual stress and stress relaxation on the fatigue life of AISI 4340 steel, Int. J. Fatigue 24 (2002) 877–886, https://doi.org/10.1016/S0142-1123(01)00205-5.
[23] X. Liu, J. Liu, Z. Zuo, H. Zhang, Numerical study on residual stress redistribution of shot-peened aluminum 7075-T6 under fretting loading, Int. J. Mech. Sci. 160 (2019) 156–164, https://doi.org/10.1016/j.ijmecsci.2019.06.031.
[24] K. Pereira, T. Yue, M. Abdel Wahab, Multiscale analysis of the effect of roughness on fretting wear, Tribol. Int. 110 (2017) 222–231, https://doi.org/10.1016/j.triboint.2017.02.024.
[25] S. Žák, J. Horníková, P. Šandera, T. Vojtek, M. Kianicová, J. Pokluda, Local and equivalent stress intensity factors for tortuous cracks under remote mode II loading, Theor. Appl. Fract. Mech. 101 (2019) 35–45, https://doi.org/10.1016/j.tafmec.2019.01.030.
[26] M. Moreno-Rubio, D. Erena, J. Vázquez, C. Navarro, Study of the shot peening surface roughness in fretting, Tribol. Int. 193 (2024), https://doi.org/10.1016/j.triboint.2024.109444.
[27] N.A. Bhatti, M.A. Wahab, Finite element analysis of fretting fatigue under out of phase loading conditions, Tribol. Int. 109 (2017) 552–562, https://doi.org/10.1016/j.triboint.2017.01.022.
[28] J. Wang, L. Yao, X. Zheng, K. Xu, S.S. Qi, X. Xiao, et al., Finite element analysis of fretting fatigue properties of GH4169 superalloy considering the surface treatments, Int. J. Fatigue 183 (2024) 108266, https://doi.org/10.1016/j.ijfatigue.2024.108266.
[29] A. Fajri, A.R. Prabowo, E. Surojo, F. Imaduddin, J.M. Sohn, R. Adiputra, Validation and verification of fatigue assessment using FE analysis: a study case on the notched cantilever beam, Procedia Struct. Integr. 33 (2021) 11–18, https://doi.org/10.1016/j.prostr.2021.10.003.
[30] B.N.J. Persson, Contact mechanics for randomly rough surfaces, Surf. Sci. Rep. 61 (2006) 201–227, https://doi.org/10.1016/j.surfrep.2006.04.001.
[31] L. Pei, S. Hyun, J.F. Molinari, M.O. Robbins, Finite element modeling of elasto-plastic contact between rough surfaces, J. Mech. Phys. Solids. 53 (2005) 2385–2409, https://doi.org/10.1016/j.jmps.2005.06.008.
[32] G. Liu, D. Zhou, J. Guo, Y. Bao, Z. Han, J. Lu, Numerical simulation of fatigue crack propagation interacting with micro-defects using multiscale XFEM, Int. J. Fatigue 109 (2018) 70–82, https://doi.org/10.1016/j.ijfatigue.2017.12.012.
[33] Q. Deng, N.A. Bhatti, X. Yin, M. Abdel Wahab, The effect of a critical micro-void defect on fretting fatigue crack initiation in heterogeneous material using a multiscale approach, Tribol. Int. 141 (2020) 105909, https://doi.org/10.1016/j.triboint.2019.105909.
[34] A. Belattar, C. Keller, L. Taleb, Multiscale analysis of the pre-hardening effect on the cyclic behavior and fatigue life of 304L stainless steel, Mater Sci. Eng. A 662 (2016) 468–480, https://doi.org/10.1016/j.msea.2016.03.093.
[35] N.R. Gates, A. Fatemi, On the consideration of normal and shear stress interaction in multiaxial fatigue damage analysis, Int. J. Fatigue 100 (2017) 322–336, https://doi.org/10.1016/j.ijfatigue.2017.03.042.
[36] B. Fodor, P. Kozma, S. Burger, M. Fried, P. Petrik, Effective medium approximation of ellipsometric response from random surface roughness simulated by finite-element method, Thin. Solid. Films. 617 (2016) 20–24, https://doi.org/10.1016/j.tsf.2016.01.054.
[37] W.N. Findley, A theory for the effect of mean stress on fatigue of metals under combined torsion and axial load or bending, J. Eng. Ind. 81 (1959) 301–305, https://doi.org/10.1115/1.4008327.
[38] L. Susmel, D. Taylor, A novel formulation of the theory of critical distances to estimate lifetime of notched components in the medium-cycle fatigue regime, Fatigue Fract. Eng. Mater. Struct. 30 (2007) 567–581, https://doi.org/10.1111/j.1460-2695.2007.01122.x.
[39] M.H. El Haddad, N.E. Dowling, T.H. Topper, K.N Smith, J integral applications for short fatigue cracks at notches, Int. J. Fract. 16 (1980) 15–30, https://doi.org/10.1007/BF00042383.
[40] D. Taylor, Predicting the fracture strength of ceramic materials using the theory of critical distances, Eng. Fract. Mech. 71 (2004) 2407–2416, https://doi.org/10.1016/j.engfracmech.2004.01.002.
[41] J. Vázquez, C. Navarro, J. Domínguez, Experimental results in fretting fatigue with shot and laser peened Al 7075-T651 specimens, Int. J. Fatigue 40 (2012) 143–153, https://doi.org/10.1016/j.ijfatigue.2011.12.014.
[42] J. Park, D. Nelson, Evaluation of an energy-based approach and a critical plane approach for predicting constant amplitude multiaxial fatigue life, Int. J. Fatigue 22 (2000) 23–39, https://doi.org/10.1016/S0142-1123(99)00111-5.
[43] Z. Cai, Weighted Nadaraya-Watson regression estimation, Stat. Probab. Lett. 51 (2001) 307–318, https://doi.org/10.1016/S0167-7152(00)00172-3.
[44] K. Pereira, T. Yue, M. Abdel Wahab, Multiscale analysis of the effect of roughness on fretting wear, Tribol. Int. 110 (2017) 222–231, https://doi.org/10.1016/j.triboint.2017.02.024.
[45] Greenwood J.A., Williamson J.B.P. Contact of nominally flat surfaces n.d.
[46] C.A. Brown, H.N. Hansen, X.J. Jiang, F. Blateyron, J. Berglund, N. Senin, et al., Multiscale analyses and characterizations of surface topographies, CIRP Ann. 67 (2018) 839–862, https://doi.org/10.1016/j.cirp.2018.06.001.
[47] K. Kalyanasundaram, P.B. Nagy, A simple numerical model of the apparent loss of eddy current conductivity due to surface roughness, NDT. E Int. 37 (2004) 47–56, https://doi.org/10.1016/j.ndteint.2003.08.005.
[48] Blodgett M.P., Ukpabi C.V., Nagy P.B. Surface roughness influence on eddy current electrical conductivity measurements 2002.
[49] C. Li, R. Karimbaev, S. Wang, A. Amanov, D. Wang, M. Abdel Wahab, Fretting wear behavior of Inconel 718 alloy manufactured by DED and treated by UNSM, Sci. Rep. 13 (2023) 1–19, https://doi.org/10.1038/s41598-023-28128-8.